Check for updates

Research Article | Vol. 32, No. 22 / 21 Oct 2024 / *Optics Express* 38203

Optics EXPRESS

Exploring the optimal combination of Ru/Ta bilayer mask stacks and illumination source shapes to mitigate mask 3D effects at high-NA extreme ultraviolet lithography

DEVESH THAKARE,[1,2,*] ANNELIES DELABIE,[1,2] AND VICKY PHILIPSEN[2]

[1] *KU Leuven Department of Chemistry, Leuven, Belgium*
[2] *imec, Kapeldreef 75, B-3001 Leuven, Belgium*
[*] *devesh.thakare.ext@imec.be*

Abstract: The imaging performance of extreme ultraviolet (EUV) lithography is determined by the optical properties and thickness of the photomask absorber material and the illumination source shape. Optimizing the trade-offs between imaging metrics, such as normalized image log slope, telecentricity error, and best focus variation through pitch (collectively known as mask-3-dimensional (M3D) effects), is crucial to improve the throughput of the EUV lithography process. This study aims to optimize Ru/Ta bilayer photomask absorber stacks and illumination source shapes to mitigate M3D effects using mask diffraction analysis. It intends to raise questions about the conventional absorber reflectivity or induced phase shift-based approach.

© 2024 Optica Publishing Group under the terms of the Optica Open Access Publishing Agreement

1. Introduction

Achieving an improved resolution to increase the transistor density in Integrated Circuits (ICs) has been a continuing endeavor in the field of semiconductor device manufacturing. Extreme Ultraviolet (EUV) Lithography has emerged as a revolutionary technology to address challenges in resolution improvement. EUV lithography tools with Numerical Aperture (NA) 0.33 are being employed in high-volume semiconductor device manufacturing, and upcoming High-NA 0.55 equipment will make it possible to print Critical Dimensions (CD) of 10 nm (and ultimately down to 8 nm) [1,2]. Although EUV lithography offers the advantage of printing smaller features due to its shorter wavelength of 13.5 nm, M3D (Mask 3-Dimensional) effects pose an imaging challenge [3]. Consequences of M3D effects are observed as contrast loss or reduced Normalized Image Log Slope (NILS), Telecentricity Error (TCE), and Best Focus Variation through pitch (BFV). The EUV photomask is responsible for delivering a perfect aerial image, ideally having a maximum contrast with zero TCE and BFV. However, researchers have attributed imperfections in the aerial image to the mask and questioned the effectiveness of the current Ta-based absorber materials for high-NA 0.55 EUV lithography [4]. As we aim to print smaller dimensions with high-NA EUVL, researchers and industry professionals are actively investigating alternative absorber materials that can potentially improve imaging [5–7]. The knowledge gained from such explorations has broadened our horizons and given us a deeper understanding of the function of the mask absorber in imaging [8–11]. These exploratory research studies have led to the development of M3D effect mitigation strategies considering the optical characteristics of the mask absorber material, in particular the refractive index n and extinction coefficient k at EUV wavelength [12].

Alloys of Ru and Ta have already been investigated under the low n or attenuated phase shifting mask category. These alloys exhibit improved EUV imaging performance but face challenges during patterning [13,14]. In a previous study, we demonstrated the patterning of the Ru/Ta

#522907 https://doi.org/10.1364/OE.522907
Journal © 2024 Received 7 Mar 2024; revised 30 May 2024; accepted 24 Jun 2024; published 8 Oct 2024

bilayer absorber approach [15]. The top layer thickness optimization in a bilayer approach is based on the thin film interference phenomenon, and the total absorber thickness optimization is determined after diffraction order analysis of the smallest pitch. In that Ru/Ta bilayer study, we focused on one particular combination of bilayer stack and illumination source. However, studies of Ta-based and TaCo alloy mask absorbers show trade-offs in imaging metrics as a function of illumination source shape [16]. Our previous learnings indicate that a particular type of illumination source shape that is best suited for a given absorber mask might not be the best choice for a different kind of absorber mask. Thus, this work aims to verify our hypothesis through imaging simulations and analyze the Ru/Ta bilayer absorber mask stacks using different illumination source shapes. Also, we do a comprehensive exploration of different possible combinations of Ru/Ta bilayer mask absorber stacks from the imaging perspective to learn potential benefits, limitations, and future directions for improving lithographic performance.

By conducting a systematic aerial image analysis of Ru/Ta bilayer absorber mask stacks and illumination source shape combinations using High-NA 0.55 exposure tool settings, we aim to provide a roadmap for identifying the most promising bilayer option and contribute to the ongoing research efforts in the field of alternative EUV absorber masks. We have aimed at a wafer level target of 10 nm Line and Space (LnS) pattern with the smallest pitch of 20 nm and 14 nm of Contact Hole (CH) square array pattern with the smallest pitch of 28 nm at High-NA 0.55 settings.

2. Methodology

2.1. Simulation setup

The S-Litho EUV software by Synopsys has been employed to perform rigorous imaging simulations by solving the Maxwell's electromagnetic equations. A Chief Ray Angle at Object (CRAO) of 5.355deg for an EUV light source having a wavelength of 13.5 nm and an anamorphic projection mirror with a radial obscuration in the center, having an radius ε=0.2 are the standard scanner inputs for High-NA 0.55 simulations [17,18]. We use the Mo/Si Multi-Layer (ML) mirror mask model described by Makhotkin et al. [19] in our simulations. Table 1 lists optical constants viz. refractive index n and extinction coefficient k for Ru and Ta at 13.5 nm wavelength. These values are as available in the S-Litho EUV software and closely resemble the CXRO (The Centre for X-Ray Optics) database. We employ the 60 nm Ta-absorber mask [19] as reference in our imaging study. In the S-Litho EUV software, the phase and amplitude of the diffraction orders have been evaluated at the mask sigma setting corresponding to the telecentric sigma of the smallest pitch. By doing this we ensure that the reported diffraction spectrum takes the incidence angle of the illumination point source into consideration.

Table 1. Optical Constants of Ru and Ta at EUV wavelength of 13.5 nm as available in the S-Litho EUV database.

Element	n	k
Ru	0.886358	0.0170689
Ta	0.94291	0.04081

The chronology of the steps used for the bilayer absorber optimization approach are as follows.

1. The thin film interference phenomena is used to determine the thickness of the top layer absorber, considering multiple orders of constructive and destructive type of interferences.
2. To determine the optimal overall absorber thickness, the thickness of the bottom layer is adjusted while the thickness of the top absorber layer is fixed. While arriving at recommended total absorber thickness, a holistic approach is followed by considering the different imaging metrics.

3. Later, we perform a comprehensive imaging performance evaluation of the selected bilayer absorber stack for LnS patterns with both horizontal and vertical orientation as well as squared CH patterns by employing different illumination source shapes. We analyse the trends in the imaging metrics as function of illumination source shapes.

2.2. Ru/Ta bilayer absorber stack thickness optimization

In this section, we briefly discuss the bilayer thickness optimization steps whose detailed description is available in Ref. [15]. The two important steps are, first, determining the optimal top layer thickness using the thin film interference phenomenon, and second, the total absorber thickness that includes both the top and bottom layers.

The top layer thickness determines the type of interference, which can be either constructive or destructive. We can calculate different top layer thicknesses leading to various orders of constructive or destructive interferences. 1st Con refers to the thinnest top layer thickness that results in constructive interference; 2nd Con refers to the next incremental absorber thickness where constructive interference reoccurs; and so on. A similar convention is followed for destructive interferences (1st Des, 2nd Des, etc.).

As thin film interference is primarily a surface phenomenon, a profound interaction between the reflected rays is expected when the top absorber layer has less absorption. Thus, Ru, a low-n, low-k material, is well suited at the top layer position.

Once the top layer thickness is fixed, we optimize the total absorber thickness using a Telecentric Sigma Point Source (TS-PS) illumination corresponding to the smallest targeted pitch. With TS-PS, the diffracted beams have symmetrical incidence angles upon arrival at the image plane and are in phase in any plane perpendicular to the propagation path. This leads to an infinite depth of focus, eliminating the focus variable necessity as NILS remains constant. Further explanation related to TS-PS can be found in Ref. [16] and formulas in Sec. 2.3.2.

At total absorber thickness optimization step, once the top layer is fixed, the bottom layer is incremented in small steps, and the mask bias is varied to achieve maximum NILS at each total absorber thickness; preferably seeking a NILS value greater than 2 for effective pattern transfer [20]. The optimum total absorber thickness is found to closely fulfill the following conditions: the zeroth and first diffraction order amplitudes are balanced, and the phase difference between them is minimum, resulting in optimum throughput (see Eq. (1) in Sec. 2.3.1). A detailed description of the absorber thickness optimization methodology adopted for this research has been published in our previous paper [16].

Frequently printed patterns include LnS and CH patterns. The orientation of LnS patterns is either horizontal or vertical. In the center slit position, the scan direction of the illuminator source of the EUV tool is orthogonal to the horizontal LnS, whereas it is parallel in the case of vertical LnS [17]. Vertical LnS will experience shadowing and a shift of the aerial image of each individual source point, but the resulting aerial image (combining all aerial images of all source points in a dipole illumination) will be symmetrical and will suffer from fading. Thus, the symmetry of the illumination source compensates for the asymmetry in the obtained images because the CRAO of the illumination source is parallel to the vertical orientation. Whereas horizontal LnS will suffer asymmetrical shadowing effects making them critical as they become susceptible to contrast loss and Telecentricity Error (TCE) [17,21] because the CRAO of the illumination source is orthogonal to the horizontal orientation. Therefore, we put emphasis on horizontal LnS during the absorber thickness optimization process.

For each order of constructive and destructive interferences, one to two prospective combinations of total absorber thickness were selected to perform a comprehensive imaging evaluation described in the following subsection.

Optics EXPRESS

2.3. Imaging performance evaluation

This subsection describes the procedure followed to evaluate the imaging performance of selected bilayer stacks using different illumination source shapes. Before explaining the procedure, let us familiarize ourselves with the imaging metrics and their criteria in this evaluation process.

2.3.1. Imaging metrics and criteria

As mentioned earlier, NILS is the primary imaging metric, which needs to be as large as possible and at least greater than 2 for effective pattern transfer. The threshold-to-size (TtS) is the aerial image intensity level at which a feature's target CD is established, and also NILS is evaluated at this threshold value. The exposure dose necessary to print on target and the TtS are inversely correlated. Based on our previous learnings, NILS exhibits trade-offs with TtS [7]. Therefore, to address this trade-off, the Throughput Criterion (TpT) (Eq. (1)) is the metric taken into consideration [22].

$$\text{Throughput Criterion (TpT)} = \text{NILS}\sqrt{\text{TtS}} \tag{1}$$

The lateral pattern shift of a feature as a function of focus is represented by TCE and is expressed in mrad or nm/um. E. Van Setten et al. [23] recommend TCE below 20 mrad to keep M3D-induced overlay errors under control, as expressed in Eq. (2).

$$M3D\ induced\ overlay = TCE\ x\ Focus\ Budget\ half\ \ range \tag{2}$$

Moving on, our next imaging metric is BFV. The best focus for a particular pitch is the focus value that produces the highest NILS. BFV is the difference between the maximum and minimum values of the best focus through pitch. To print the different patterns with the largest overlapping process window, BFV must be as small as possible. A total focus budget of 35 nm is the goal for high NA EUV lithography [24]. Considering this fact and referring to Eq. (2), having TCE and BFV as small as possible becomes a critical condition at High-NA.

2.3.2. Evaluation procedure

Next, we return to our topic, the imaging performance evaluation of selected bilayer stacks using different illumination source shapes. Our primary source from which other illumination sources are derived is a Leaf shape Dipole (LDP), the dark region formed by the overlap of the zeroth and first diffraction orders, as illustrated in Fig. 1. The illumination source shape can be considered as a collection of many point sources that compose a desired shape. In the full leaf shape dipole, each leaf pole is symmetric around σTC, which is the telecentric sigma of the smallest pitch (20 nm), as shown in Fig. 1. The telecentric sigma is computed using Eq. (3) for equal LnS patterns and Eq. (4) for CH in a square array [16].

$$\text{Telecentric}\sigma\text{forLnS} = \frac{\lambda}{2\ \text{NA P}} \tag{3}$$

$$\text{Telecentric}\sigma\text{forCH} = \frac{\lambda}{\sqrt{2}\ \text{NA P}} \tag{4}$$

where σ indicates the position of the point source in the pupil plane, λ denotes the illumination wavelength, NA is the numerical aperture, and P is the pattern pitch.

Other illuminations source shape viz. Inner Half Leaf shape Dipole (IHLDP), Outer Half Leaf shape Dipole (OHLDP), and Mid Leaf shape Dipole (MLDP) are created out of the LDP by blocking necessary parts.

The source shapes are classified based on the distribution of the point sources relative to the telecentric sigma of the smallest pitch (σTC ~ 0.6136). IHLDP represents a collection of inner sigma source points of the LDP, i.e., sigma values ≤ σTC, OHLDP represents a collection

Optics EXPRESS

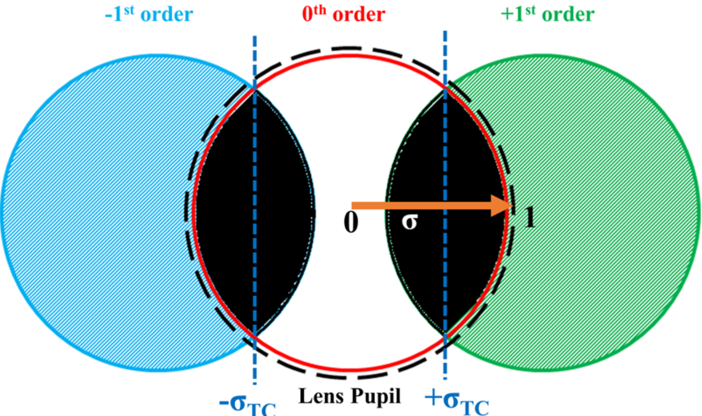

Fig. 1. A Schematic representing the formation of a leaf shape dipole (LDP) illumination source shape. The black dashed circle represents the lens pupil, and any diffraction order components that fall inside this region will contribute to imaging. The red circle and its enclosed area are a set of all zeroth diffraction order representation, resulting from the interaction between a mask with a vertical LnS pattern with a certain pitch and circular illumination source (comprising of many point sources). Similarly, the blue and green regions represent the set of all -1st and +1st diffraction orders, respectively. σ indicates the position of the point source in the pupil plane, which ranges from 0 to 1, covering the radial distance. σTC is the telecentric sigma corresponding to the smallest pitch about which the leaf is symmetrical.

of outer sigma source points of the LDP, i.e., sigma values ≥ σTC, and MLDP represents a collection of source points of the LDP distributed around the telecentric sigma (with 0.22 sigma width) corresponding to the smallest targeted pitch. Since a pupil-fill ratio of 20% is essential for maximum productivity, an effort was made to maintain this minimum standard [25]. Illumination source shapes for horizontal LnS are depicted in Fig. 2, and for vertical LnS are depicted in Fig. 3.

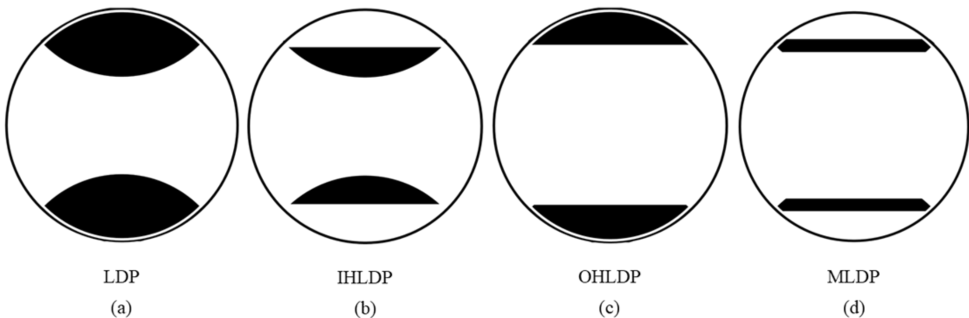

Fig. 2. Schematic representation of illumination source shapes used for horizontal LnS simulations (not to the scale)

Similarly, for the imaging performance evaluation of CH, we employed Full Quasar Pole (FQP) centered around the telecentric sigma of the smallest CH pitch, Inner Quarter Quasar Pole (IQQP), and Outer Quarter Quasar Pole (OQQP) as shown in Fig. 4. The illumination source choice is made as per recommendations of Franke et al. [26].

After choosing the illumination source shapes, we move on to evaluating NILS using different mask biases for each absorber mask stack and illumination source combination. At this stage,

Optics EXPRESS

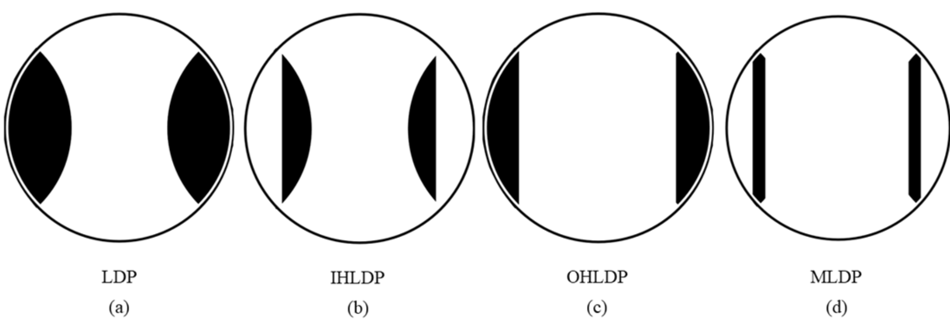

Fig. 3. Schematic representation of illumination source shapes used for vertical LnS simulations (not to the scale)

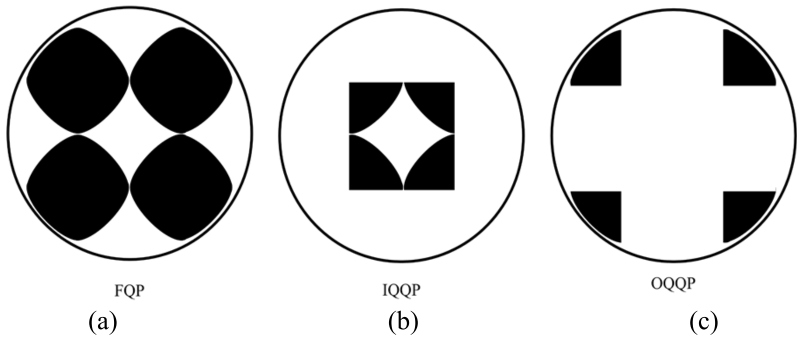

Fig. 4. Schematic representation of illumination source shapes used for CH simulations (not to the scale)

we have focused on horizontal LnS patterns. We anchor the TtS value corresponding to the mask bias that results in maximum NILS. The calculated NILS, TCE, and TpT values for the smallest CD target at the TtS are used for the assessment. Utilizing the anchored TtS and varying the wafer focus, we calculate the bias for larger pitches that can print the 10 nm target at the wafer level with a ± 10% tolerance. We concentrate on dark field horizontal LnS patterns while evaluating the BFV behavior.

Later, we tabulate the simulation results of all imaging metrics obtained for selected bilayer stacks and illumination source combinations. Then, we compare their performance against the current 60 nm Ta-based absorber mask. Assessment of this data intends to identify one or two Ru/Ta bilayer stacks that exhibit optimized performance based on criteria mentioned in the previous subsection.

Further, those Ru/Ta bilayer stacks exhibiting a promising result in the mentioned above assessment, will be selected to perform a detailed study. A through-pitch evaluation is carried out to study the impact of different illumination source shapes on imaging metrics for Ru/Ta bilayer stacks. At this stage, we consider horizontal and vertical LnS patterns and CHs. We investigated pitch ranging from 20 nm to 40 nm with a 4 nm increment for LnS patterns and pitch 28 nm, 32 nm, 36 nm, 42 nm, and 56 nm for CH patterns.

Next, we will divert our attention to comprehend the BFV behavior. From previous studies, it is a known fact that the BFV largely depends on the illumination source shape [16]. Therefore, it would be intriguing to investigate the relationship between the BFV and the position of the source points in terms of pupil sigma. We decided to investigate vertical LnS patterns through pitch since they are not prone to asymmetrical shadowing, rendering a simplified interpretation

of trends. We undertook a simulation exercise to study the best focus trends by utilizing a dipole line source whose position varies through sigma (Fig. 5). For certain pitches, point sources placed along the line dipole shown in Fig. 5, the central obscuration will block diffraction orders. However, the remaining part of such diffraction order will still contribute to image formation. We will keep this in mind when interpreting the results. We anchored TtS corresponding to the LDP and varied the line source position from inner to outer sigma over the LDP source shape (optimized to the smallest pitch). This approach is expected to give a better perception about the response of each line source and the way it impacts the mask bias at a given TtS value representing the full LDP shape. The sigma position of the line source was varied from 0.26 (inner) to 0.96 (outer). The mask trench width and focus were varied for each pitch and line source combination to determine the bias that can print on target with ±10% tolerance.

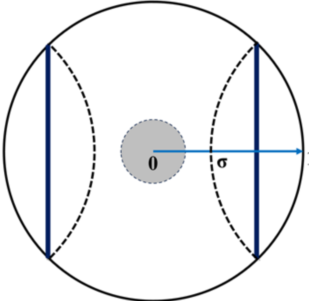

Fig. 5. A schematic illustration of a dipole line source whose position changes from inner to outer sigma over the LDP source shape. The circle in the center represents the area where the diffraction orders would be blocked in the pupil plane. The width of the line source is 0.01 sigma. Alternatively, it can be viewed as an "and" operation of mathematical logic between the LDP and the line source, as the line source moves over sigma positions from inner to outer.

3. Results and discussions

3.1. Determining top Ru layer thickness

As stated previously in the methodology section, the first step is to determine the top Ru layer thickness for different orders of interferences. The list of the interference orders and corresponding top Ru layer thicknesses for high NA tool settings, can be found in second column of Table 2 in the next subsection. We have limited our scope till the 5th order of interference.

3.2. Determining the total thickness of prospective bilayer absorber stacks

After determining the top Ru layer thicknesses, we optimize the total absorber thickness by varying the bottom Ta layer. The procedure followed to arrive at the recommended absorber thickness has been briefly described in the methodology section. For a detailed description, we recommend Ref. [16]. Figure 6(a) shows the NILS as a function of the absorber thickness for a horizontal LnS pattern with a wafer level target of 10 nm having 20 nm pitch for three representative Ru/Ta bilayer stacks and the reference Ta-based absorber. The amplitude ratio of first diffraction orders to zeroth diffraction orders and cosine of the phase difference between first diffraction order and zeroth diffraction orders is illustrated for selected Ru/Ta bilayer absorber stacks in Fig. 6(b), (c), and (d). Reported NILS values are using a TS-PS illumination, and the diffraction order analysis is obtained at the mask sigma setting of the S-Litho EUV software, corresponding to the telecentric sigma of the smallest pitch.

Optics EXPRESS

Table 2. List of selected bilayer absorber mask stacks with their respective reflectivity and induced phase shift (considering an ML mirror below)

Interference Order	Top Ru	Bottom Ta	Total Absorber Thickness	Absorber Reflectivity	Phase Shift
	nm	nm	nm	%	degrees
1st Con	3.8	49	52.8	0.75	226.5
1st Des	7.6	52	59.6	0.52	229.5
2nd Con	11.5	42	53.5	0.68	240.4
2nd Des	15.3	38	53.3	1.21	221.9
3rd Con	19.2	35	54.2	0.74	251.1
3rd Des	23.0	31	54.0	1.61	243.9
4th Con Thick	26.8	28	54.8	1.05	263.6
4th Con Thin	26.8	20	46.8	4.35	246.5
4th Des Thick	30.6	24	54.6	2.22	266.5
4th Des Thin	30.6	16	46.6	5.62	246.2
5th Con Thick	34.5	21	55.5	1.65	279.0
5th Con Thin	34.5	13	47.5	5.44	266.9
5th Des Thick	38.4	18	56.4	3.43	279.6
5th Des Thin	38.4	9	47.4	7.06	270.0
TaBN reference	–	–	60	1.29	156.3

The saturation point in the NILS swing behavior happens when the corresponding diffraction order amplitude ratio and cosine of phase difference are close to one (Fig. 6(a-d)). Considering this fact, we select a couple of bilayer absorber stacks to perform a detailed imaging analysis using different illumination source shapes, as mentioned in Sec. 2.3.2.

Let us explain the selection procedure through an example. In Fig. 6(b), at the point highlighted with the dashed vertical line, the amplitude ratio of -1st to 0th diffraction is close to one, and the cosine of the phase difference of -1st and +1st to 0th diffraction orders is also close to one. We observe a NILS peak at the corresponding absorber thickness for the Ru/Ta 2nd Des absorber stack in Fig. 6(a). Thus, we select 15.3 nm of the top Ru layer with 38.0 nm of the bottom Ta layer, making the total absorber thickness 53.3 nm. We will refer to this as "Ru/Ta 2nd Des" from here onwards (unless explicitly specified).

A similar procedure is followed to decide the prospective bilayer absorber thickness corresponding to other interference orders. For the first three orders of the interferences, one prospective bilayer stack has been selected for further investigation. However, we picked two variations for the fourth and fifth interference orders, a thick and a thin absorber stack, as both showed promising improvement in NILS. The selected thick and thin variations from the 4th Con and 4th Des order of interference are as illustrated by dashed lines in Fig. 6(c) and (d), respectively. We want readers to pay attention to the diffraction order properties at the two selected thicknesses marked with red and black dashed lines in Fig. 6(c) and (d). It will help us understand the imaging performance trends discussed in the next section. The final list of Ru/Ta bilayer absorber stacks selected to evaluate the imaging performance is presented in Table 2. Vertical LnS pattern analysis was also considered during the absorber thickness selection process. Although reflectivity and induced phase shift are not the selection criteria, they are listed for the reader's additional information in Table 2.

Optics EXPRESS

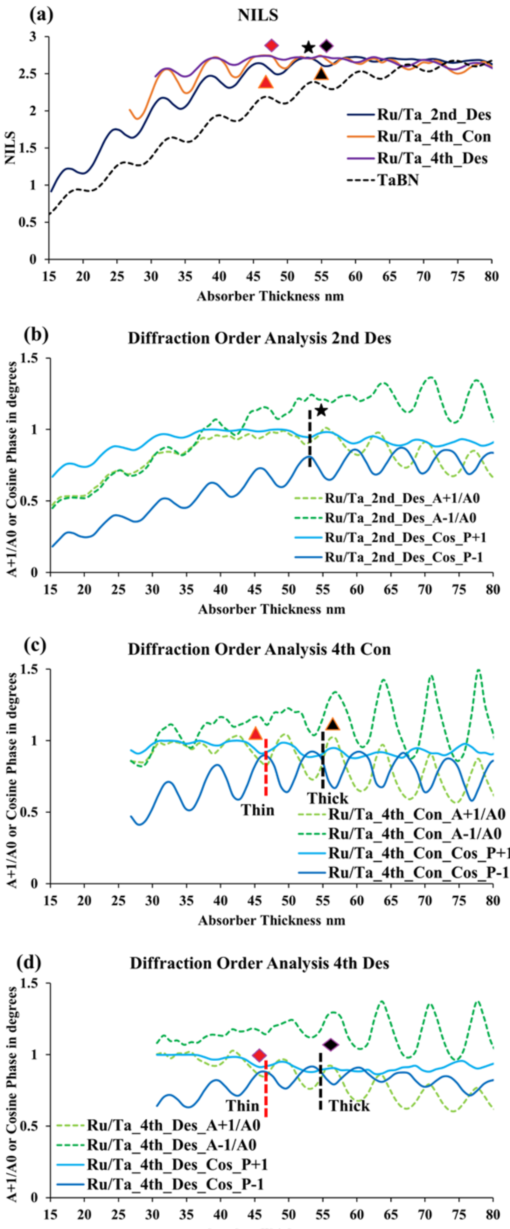

Fig. 6. Imaging metric and diffraction order analysis of horizontal LnS with a wafer level target of 10 nm having 20 nm pitch using a TS-PS illumination (a) NILS as a function of total absorber thickness for specified bilayer absorber stacks and reference Ta-based absorber. Amplitude ratio and cosine of the phase difference between first and zeroth diffraction order of (b) 2nd Des, (c) 4th Con, and (d) 4th Des order of interference of the Ru/Ta bilayer. The selected thick and thin variations from the 4th Con and 4th Des order of interference are as illustrated by dashed lines. The marked absorber thickness corresponds to the local peaks in the NILS swing plot of respective absorber stacks.

3.3. Imaging performance evaluation of selected bilayer stacks

Moving on, we evaluate the imaging performance of the bilayer stacks listed in Table 2 using four different illumination sources, viz. LDP, IHLDP, OHLDP, and MLDP. At this stage, we focus on a horizontal LnS pattern with a wafer-level target of 10 nm. A detailed comparison of the imaging simulation results for selected bilayer stacks and reference Ta-based absorbers can be found in Supplement 1. The imaging metric reported corresponds to the smallest pitch of 20 nm. The pitch is varied from 20 nm to 40 nm to calculate BFV. Generic observations made against the Ru/Ta bilayer stack from the imaging data are discussed below.

The IHLDP illumination source leads to higher NILS in comparison with the OHLDP, LDP, and MLDP illumination sources. Franke et al. [25] have explained fading results from the superimposition of aerial images from different illumination poles that have been shifted against each other. Thus, NILS reduction in the case of the LDP and MLDP illumination sources is a consequence of the fading effect, but it is not as prominent as in the case of the reference Ta-based absorber (See Supplement 2). This is because the shift in the individual aerial images created by each dipole is smaller in the case of low-n materials and negligible in the case of vacuum phase matching materials [4]. Since Ru is a low-n material, the effective refractive index of the bilayer stack is expected to be lower than the Ta-based absorber. Compared to Ta-based absorbers, the improved trend in NILS for Ru/Ta bilayer stacks appears in agreement, as presented by A. Erdmann et al. [4]. A generic observation is that NILS values exhibit a moderate improvement as we increase the top Ru layer thickness from 1st order interference to 4th order interference. Thereafter, a slight drop in NILS is observed for 5th order interference. Many factors acting simultaneously would be responsible for this behavior, mainly the imbalance in the intensities of diffraction orders caused by the absorber materials' optical properties and thickness. Thus, we restrict the scope of our study until the 5th order of interference.

The next imaging metric we discuss is TCE. The MLDP illumination source leads to the smallest TCE as the source points are spread around the telecentric sigma point corresponding to the smallest pitch (See Supplement 1). The IHLDP illumination source leads to lower TCE in comparison with the OHLDP illumination source, as expected. In the case of IHLDP, the two half poles' proximity to the CRAO results in a reduced imbalance of diffraction order intensities, resulting in a lower TCE. On the other hand, the two half poles in the case of OHLDP are placed at the extreme incidence angles, leading to an intensity imbalance in diffraction orders, resulting in increased TCE. In addition, we can observe some local trends in TCE behavior (See Supplement 1). In the case of IHLDP, the thick absorber exhibits lower TCE than its thin absorber variation counterpart (4th and 5th order of interference). In contrast, in the case of LDP, OHLDP, and MLDP, a thick absorber exhibits higher TCE than its thin absorber variation counterpart. So far, we know that telecentricity error results from an imbalance in intensity between the diffracted orders [23]. The observation in this particular scenario results from several factors acting simultaneously, viz. the illumination source shape and its incidence angle, mask bias, absorber's optical properties, and thickness, which makes it challenging to disentangle the effect caused by one factor from another. Providing a clear understanding would need further research.

Turning now our discussion to BFV, the LDP illumination source exhibits relatively low BFV compared to other illumination sources (See Supplement 1). From 1st to 3rd order of interferences, the IHLDP illumination source results in lower BFV when compared to the OHLDP illumination source, except in the case of 3rd Con. From 4th order interference onwards, this trend in BFV reverses. The IHLDP illumination source leads to higher BFV when compared to the OHLDP illumination source, which is similar to the behavior of the Ta-based reference absorber with a 60 nm thickness. Other studies have reported similar behavior for the reference and high-k absorber combined with inner/outer sigma source points [7,27]. The MLDP illumination source leads to the highest BFV, as compared to the other illumination sources, for a given bilayer stack.

Optics EXPRESS

Comparing the BFV for thin and thick absorber variations, we observe that thin absorber stacks have higher BFV compared to thick absorber stacks. These observations are in agreement with those made by J. Finders et al., [28] who noted that the best focus range decreases as the thickness of Ta-based absorbers increases. We can correlate the BFV of our thick and thin bilayer absorber stacks with their respective diffraction order phase relationships. The cosine of the phase differences for thick absorber stacks are closer to 1 in comparison with their thin counterpart, especially for -1st order which demonstrates upward swing behavior in the thickness range of 30 nm to 60 nm (Fig. 6(c) and (d)). Thus, apart from the NILS gain and proper balancing of the diffraction order amplitudes, the diffraction order phase properties must also be given a significant attention while determining the optimum absorber thickness. Although there is no significant difference between the NILS values of the thick and thin variants in this case, a thick absorber variant is recommended as the diffraction order phase properties result in lower BFV. Opting for an absorber stack that exhibits a reduction in BFV is especially important considering the limited focus budget of 35 nm at a High-NA 0.55 application. The focus budget could be described as the permissible range of focus variations that may occur throughout the manufacturing process, taking into account potential significant contributors to focus errors, while ensuring sufficient pattern fidelity on the semiconductor wafer [29]. We will understand the BFV and the trends through pitch in more detail using a line source through sigma in Sec. 3.4.3.

The next step is identifying the optimal option amongst the investigated bilayer stacks. We start with the promising IHLDP illumination source. The data from Supplement 1 has been summarised by means of a bubble chart representation, as shown in Fig. 7.

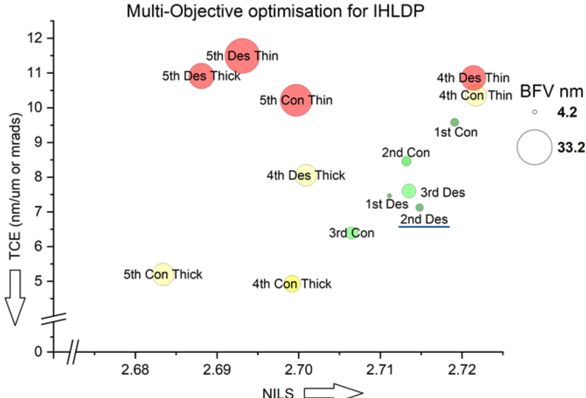

Fig. 7. Bubble chart representation of the imaging metrics analysis. A small bubble size represents smaller BFV whereas a larger bubble size represents larger BFV. The smallest bubble size is 4.2 nm, corresponding to 1st Des absorber stack, and the biggest bubble size is 33.1 nm, corresponding to 5th Des thin bilayer absorber stack. The colour green denotes traits that are more favorable with preferred ones represented in darker shade, yellow denotes traits that are moderately favorable, and red denotes traits that are least favorable. The selected 2nd Des bilayer stack has been underlined.

We seek a Ru/Ta bilayer stack that exhibits higher NILS, lower TCE, and reduced BFV (smaller bubble size having darker shades of green); this leads into multi-objective optimization. We, therefore, employ the multi-objective optimization technique that A. Erdmann et al. [5] adopted to find a non-dominant solution. Solutions for which the objective function value cannot be improved without compensating another objective function value are considered as non-dominated solutions.

From Fig. 7, we conclude that 2nd Des, 4th Con Thin, and 4th Con Thick are the non-dominant solutions. As mentioned in the previous paragraph, we recommend a thick variant demonstrating

reduced BFV, disqualifying the 4th Con Thin bilayer stack. Comparing the 2nd Des with the 4th Con Thick variant, the 2nd Des offers improved NILS and lower BFV, although the TCE is slightly higher but less than 10 mrads [23]. We, therefore, decide to proceed with the 2nd Des thick bilayer absorber stack, as it shows the most promising combination of different metrics.

3.4. Through-pitch imaging performance evaluation of 2nd Des bilayer stack

Having made the selection of the 2nd Des bilayer stack in the previous section, we move on to its through-pitch imaging performance evaluation for horizontal LnS, vertical LnS, and CH patterns using the different illumination source shapes mentioned in Sec. 2.3.2.

3.4.1. Horizontal LnS

A through-pitch imaging performance comparison for horizontal LnS pattern targeting 10 nm wafer CD and using LDP, IHLDP, OHLDP, and MLDP illumination sources is displayed in Fig. 8. The mask bias employed is shown in Fig. 8(f), and TtS at which the imaging metrics are evaluated is presented in Fig. 8(b).

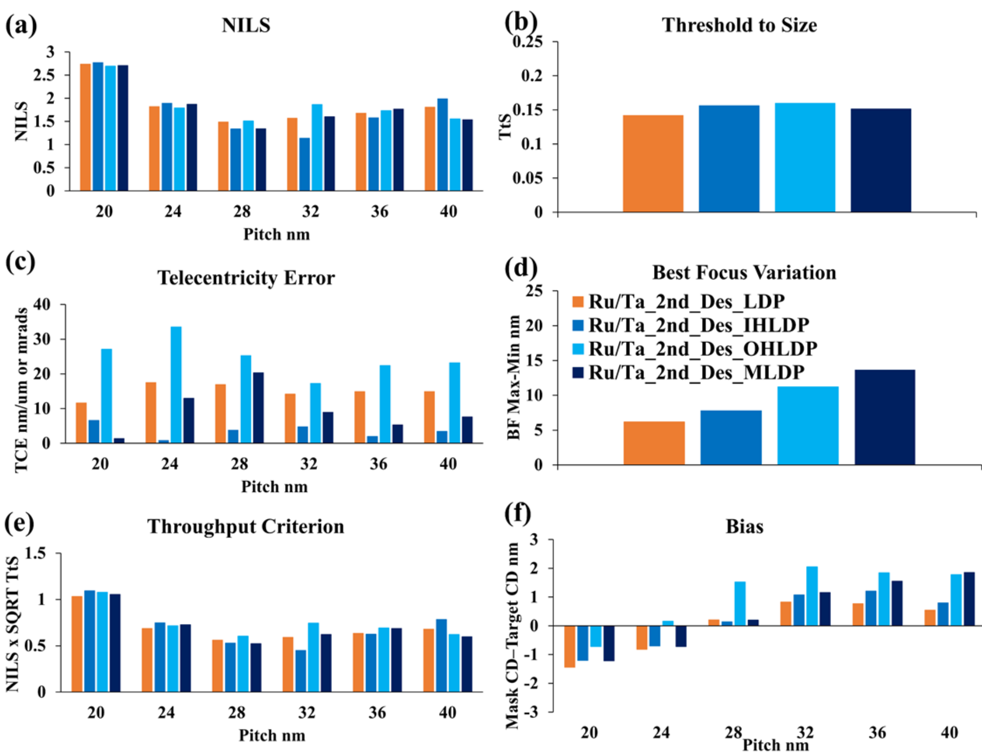

Fig. 8. A through-pitch imaging performance comparison of 2nd Des bilayer stack absorber for horizontal LnS pattern using different illumination source shapes (a) NILS, (b) Threshold-to-Size, (c) Telecentricity Error, (d) Best Focus Variation, (e) Throughput Criterion (f) Bias.

Starting with the NILS plot, we observe the highest NILS value for the smallest pitch and the lowest NILS value at the pitch of 32 nm for the IHLDP illumination source (Fig. 8(a)). The generic trend observed in NILS behavior is quite similar to those observed in the case of reference Ta-based absorbers and other novel absorber studies [7,16]. The NILS decreases as the pitch increases from pitch 20 nm to pitch 28 nm because only the 0th and ±1st diffraction orders are

Optics EXPRESS

captured, with an increasing imbalance between the amplitudes and phase difference between them. At pitch 32 nm, the IHLDP illumination source exhibits the lowest NILS due to diffraction limitation, whereas the OHLDP illumination source exhibits improved NILS in comparison to IHLDP as second diffraction orders are captured [16]. As we move from pitch 32 nm onwards, higher orders are captured, which justifies the upward trend in NILS. Generic trends in NILS behavior through pitch due to tool settings (NA and central obscuration) remain similar. Our previous research with TaCo alloy absorbers has discussed these trends in detail [16]. As the optical properties of the absorber material impact the diffraction order characteristics, the absolute values in the case of each absorber stack differ. Specifically, absolute NILS values at each pitch majorly depend on the illumination source shape and the number of diffraction orders captured (diffraction orders hitting the central obscuration region are lost and do not contribute to imaging). It appears that the LDP illumination source produces moderate NILS values throughout.

Moving on to TtS (Fig. 8(b)), we see that the IHLDP and OHLDP illumination sources exhibit slightly higher TtS because of more open bias than the LDP and MLDP illumination sources (Fig. 8(f) pitch 20 nm). This trend is opposite to that of the reference Ta-based absorber (See Supplement 2). An open bias implies that the trench on the mask, exposing the ML mirror, is comparatively wider [30].

Turning now to TCE (Fig. 8(c)), we observe modestly low values through pitch when using the IHLDP illumination source. However, when using the MLDP illumination source, we observe the lowest TCE at the smallest pitch, without any consistent trend throughout pitch. The OHLDP illumination source shows the highest TCE at all considered pitches. As the LDP is a composite of IHLDP and OHLDP, the LDP illumination source leads to a modest TCE. The explanation for these observations is stated earlier in TCE discussions of Sec. 3.3.

Next, we shift our attention to BFV (Fig. 8(d)). The LDP illumination source demonstrates the lowest BFV, followed by IHLDP, OHLDP, and MLDP. The trends in BFV are strikingly different from those observed with the reference Ta-based absorber (See Supplement 2). In the case of the Ta-based reference absorber, the IHLDP illumination source shows increased BFV as compared to the OHLDP illumination source, whereas in our case of the 2nd Des Ru/Ta bilayer stack, it is the opposite [27]. This relates to the optical properties of the absorber stack controlling the diffraction order properties, especially the phase difference. Observations made here are for the dark field mask, whereas a bright field mask is expected to show different trends [31]. Discussion related to the bright field mask is out of the scope of the current paper. Note that we will try to comprehend the BFV behavior in detail using a line source through sigma for the dark field mask in Sec. 3.4.3.

Lastly, we arrive at the discussion on TpT (Fig. 8(e)). Since there is no significant difference in TtS values amongst the illumination source shapes, TpT almost follows similar trends as the NILS plot. At the smallest pitch, we see slightly higher TpT for IHLDP and OHLDP when compared to LDP and MLDP due to their respective higher TtS.

Summarizing for horizontal LnS patterns, the LDP and IHLDP illuminations exhibit trade-offs, but both appear as good options for the 2nd Des Ru/Ta bilayer absorber stack. They lead to moderate NILS through pitch, TCE below 20 mrad, and lower BFV. Considering overall through-pitch imaging performance, the LDP illumination source could be an optimal choice, considering better NILS at pitch 32 nm and a lower overall BFV compared to IHLDP.

3.4.2. Vertical LnS patterns

A similar through-pitch imaging performance comparison for vertical LnS patterns is displayed in Fig. 9. In the NILS plot (Fig. 9(a)), we observe the highest NILS value for the smallest pitch for all illumination source shapes and the lowest NILS value at the pitch of 32 nm, particularly for the OHLDP illumination source. We see almost similar trends as described for the horizontal LnS patterns, except for the OHLDP illumination source. In the case of OHLDP, the NILS

Optics EXPRESS

value drops significantly for larger pitches. Two factors that influence the observed outcome are the presence of central obscuration [16] and a relatively higher TtS (when compared to other illumination source shapes and the reference Ta-based absorber (See Supplement 3), since NILS and TtS often exhibit trade-offs, the second factor is most likely to play a significant role as we do not observe a rising trend in NILS as we move from pitch 32 nm to pitch 40 nm in the case of OHLDP, which we do observe in case of reference absorber (See Supplement 3). A careful observation of Fig. 9(f) indicates that the open bias required to print on target using OHLDP at its anchored TtS is much higher than the rest of the illumination source shapes.

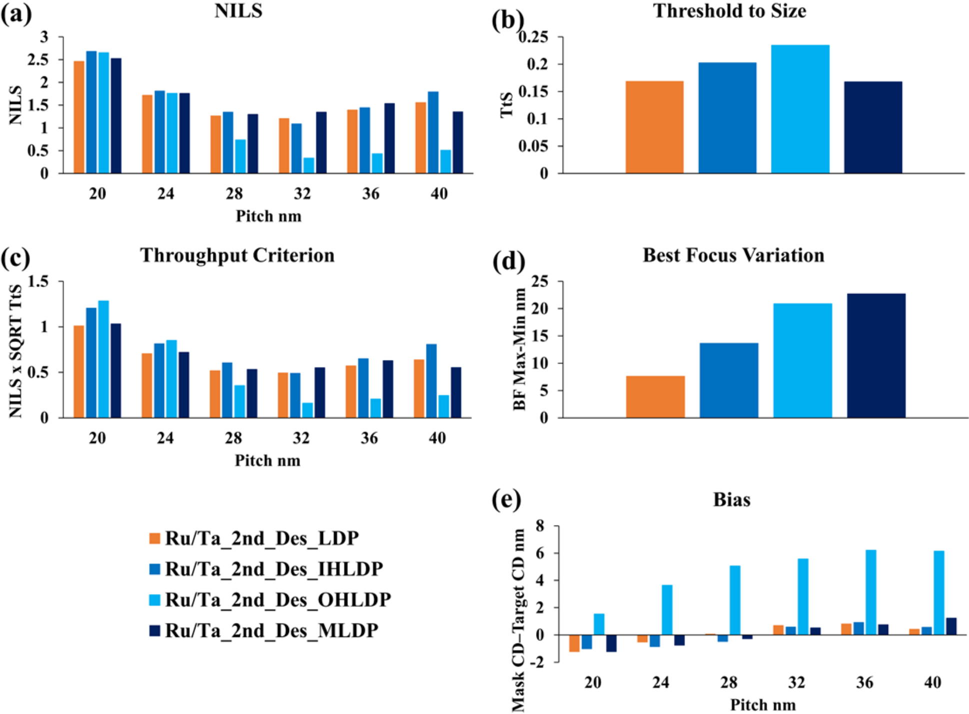

Fig. 9. A through-pitch imaging performance comparison of 2nd Des bilayer stack absorber for vertical LnS pattern using different illumination source shapes (a) NILS, (b) Threshold-to-Size, (c) Throughput Criterion, (d) Best Focus Variation, (e) Bias.

The IHLDP illumination source leads to higher NILS through pitch except at a pitch of 32 nm. A possible explanation for the lowest NILS at 32 nm pitch is similar to that stated for horizontal LnS patterns: because pitch 32 nm is mainly diffraction limited (higher orders are not well captured and a tiny part of first diffraction order falls in central obscuration) [16]. Unlike the horizontal LnS patterns, the IHLDP and OHLDP illumination sources show slightly more improvement in NILS at the smallest pitch for the vertical LnS patterns. With a slight improvement, the behavior for the vertical LnS patterns becomes similar to the reference Ta-based absorber (See Supplement 3), as expected due to the intrinsic lower refractive index of Ru. The LDP illumination source delivers modest NILS through pitch compared to other illuminations. NILS at the smallest pitch of the vertical LnS patterns is slightly lower than that of horizontal LnS patterns. Thus, we have to concede that vertical LnS patterns could be more susceptible to M3D effects than horizontal LnS patterns, likely due to the magnification factor [32,33]. Indeed, vertical LnS patterns undergo a 4X demagnification, whereas horizontal LnS patterns undergo 8X demagnification (anamorphic projection), which influences their respective imaging metrics;

indicating that waveguide modes observed in EUV absorbers have an impact [34]. However, a through-thickness diffraction order analysis of the vertical LnS pattern (See Supplement 4) reveals that at any absorber thickness, the necessary condition of diffraction order properties (amplitude ratio and cosine of phase difference both close to 1) that results in maximal NILS will never be fulfilled.

Before moving on to TtS, we briefly discuss the BFV through-pitch trends (Fig. 9(d)). The LDP illumination source leads to the lowest BFV, followed by IHLDP, OHLDP, and MLDP, similar to horizontal LnS, as discussed in Sec. 3.4.1. LDP and IHLDP demonstrate lower BFV for the Ru/Ta bilayer stack than the reference Ta-based absorber (See Supplement 3).

Turning now to TtS (Fig. 9(b)), although OHLDP has higher TtS than other illumination source shapes, this benefit is hampered by low NILS at larger pitch and increased BFV. Having a higher TtS could not improve TpT for OHLDP (Fig. 9(c)).

Summarizing for vertical LnS, LDP seems again an optimal choice with optimum NILS through pitch and lowest BFV.

The diffraction analysis of vertical LnS patterns suggests that imaging performance may be improved if we opt for a thicker absorber. However, in that case, the performance of horizontal LnS patterns is expected to degrade due to the increased shadowing effect, which is discussed in Supplement 5.

3.4.3. Understanding BFV shifts

In this subsection, we discuss the response of best focus behavior for different pitches when a dipole line source position is varied over an LDP illumination shape optimized for the smallest pitch. The best focus values of different pitches for the reference Ta-based absorber mask and the Ru/Ta bilayer 2nd Des absorber mask stack are displayed in Fig. 10(a) and (b), respectively. The mask biases that print 10 nm target at the wafer level are shown in Fig. 10(c) and (d), and corresponding NILS values evaluated at their respective best focuses are reported in Fig. 10(e) and (f).

Comparing Fig. 10(a) with (b), we can infer that the best focus values of each pitch depend on the absorber material as well as on the illumination shape. The telecentric sigma for each pitch is different. The best focus values have a negative sign if the source points are placed on the inner side of the telecentric sigma, whereas they typically have a positive sign if they are placed on the outer side, especially for the pitches where only two diffraction orders contribute to imaging (pitch 20 to 28 nm and in few cases for pitch 32 nm). In the case of the reference Ta-based absorber, the transition from negative focus values to positive focus values is sharp and happens at the telecentric sigma of the respective pitch (in this particular case, it is less than 0.6136; telecentric sigma for the smallest pitch of 20 nm). Thus, looking through pitch, we observe a larger BFV for small sigma sources, corresponding to IHLDP, in the case of the Ta-based absorber. These trends in BFV are similar to those observed by M. Burkhardt et al. [27] at NA 0.33 for the Ta-based absorber.

For the Ru/Ta bilayer absorber, the deviation in best focus values as a function of the line source position with respect to sigma is relatively low. This justifies the reduced BFV, especially when using the IHLDP illumination source. Nevertheless, the sigma points at which the transition happens from negative to positive best focus value depends on the pitch, as it is diffraction-based. For the MLDP illumination sigma region (Fig. 10(b)), pitch 24 and 28 nm have positive best focus values, whereas pitch 32 to 40 has negative focus values, giving rise to larger BFV (cf. Figure 9(d)). In the case of sigma 0.8 onwards at pitch 28 nm, the 2nd diffraction order is captured, but the major part of the 1st diffraction order gets blocked by the central obscuration (because of the line source shape). The simulator's algorithm tries to print on target by opting for a larger mask bias to compensate for the significant portion lost in the central obscuration of the 1st diffraction orders. Thus, this drift in the mask bias will influence the diffraction order phase

Optics EXPRESS

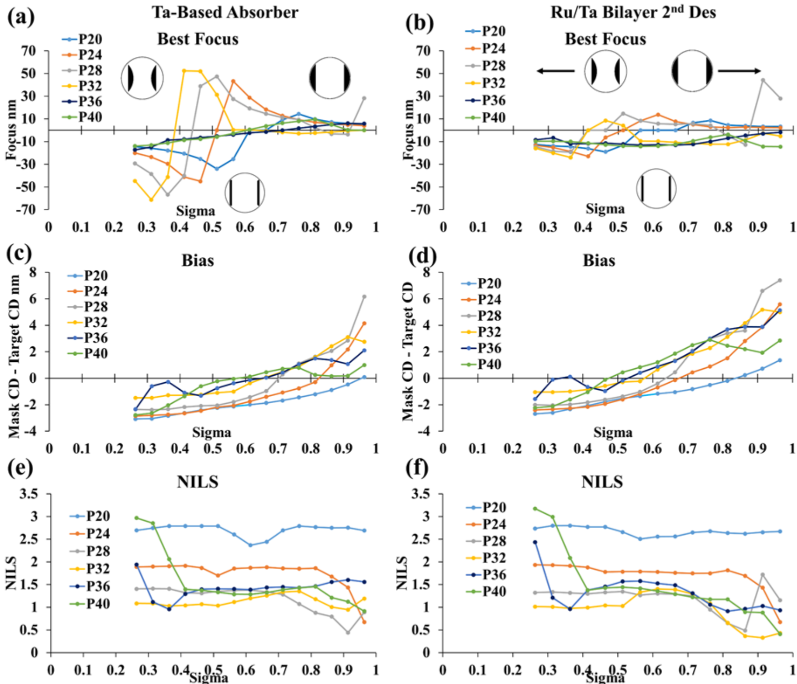

Fig. 10. A through-pitch analysis of vertical LnS pattern using a line source that varies through sigma (cf. Figure 5 in Sec. 2.3.2). The results obtained for the Ta-based absorber are shown in the left column and the 2nd Des bilayer absorber mask in the right column for the following imaging metrics: (a), (b) best focus; (c), (d) mask bias;(e), (f) NILS. In the best focus plots, a visual representation indicating where IHLDP, OHLDP, and MLDP shapes belong with respect to sigma is shown.

relationship, which might have led to an abrupt deviation in the focus value rather than a gradual change around 0.9 sigma (Fig. 10(b), pitch 28 nm) (in addition to absorber's optical properties). Additional supporting information related to the impact of central obscuration on mask bias and best focus values at pitch 28 nm and 32 nm is available in Supplement 6.

A comparison of Fig. 10(c) with (d) shows that the required bias to print on target for a Ru/Ta bilayer absorber is larger than that for the reference Ta-based absorber, which is as expected for low-n materials [35]. The difference in the biases of the two absorbers further increases as we move from inner sigma towards outer sigma. This also justifies the more open bias for OHLDP (cf. Figure 9(e)). It seems that two factors might be acting simultaneously, leading to a larger open bias at larger sigma values; first, in the case of the large angle pole at large sigma vs. the small angle pole at small sigma, the increased shadowing from the large sigma line dipole is compensated by a more open mask bias than for the smaller sigma line dipole. Second, a larger mask bias is expected to compensate for the loss of the diffraction orders blocked by the central obscuration for certain pitch and sigma combination scenarios, to ensure printing on target.

Lastly, in this subsection, we throw some limelight on the NILS plots (Fig. 10(e) and (f)). In Fig. 10(e), the NILS value for a pitch of 20 nm is high for inner and outer sigma values. Fading causes a NILS drop around each pitch's telecentric sigma value [26]. This is because the shift in the image formed by individual poles is a consequence of the optical properties of absorber material, which is more significant in the case of reference Ta-based absorber. The image shift is lesser in the case of the Ru/Ta bilayer absorber stack compared to the reference Ta-based absorber; hence, a low fading effect is observed. The fading effect remains in the telecentric

Optics EXPRESS

sigma due to the mask absorber phase, while for the other sigma values, wafer focus can be adjusted to minimize the fading [26]. At pitch 24 nm, some parts of 1st diffraction order are blocked by the central obscuration corresponding to extreme outer sigma, which justifies the drop in NILS for sigma greater than 0.8 [16]. The 2nd diffraction order starts interfering for extreme outer sigma values at pitch 28 nm and inner sigma values at pitch 32 nm [16]. A reduction in NILS is observed for pitch and line source combinations whose first diffraction order hits the central obscuration. This justifies the rise and fall trends in NILS as we advance from inner sigma to outer sigma values for larger pitches.

Although we are aware that the optical properties of the absorber material, its thickness, and the incidence angle of the illumination source (which varies as per the position of the point sources) control the diffraction order properties, it is less apparent to predict the generic trends without the aid of rigorous simulations because they are highly case-specific.

3.4.4. Contact holes

A through-pitch imaging performance comparison of CH pattern in a square array targeting 14 nm wafer CD and using FQP, IQQP, and OQQP illumination sources (cf. Figure 4) is displayed in Fig. 11. The mask bias employed is shown in Fig. 11(f). TtS at which the imaging metrics are evaluated along the horizontal cutline is as appearing in Fig. 11(b). For simplicity, we restrict the mask biasing to square CH, i.e., the same mask bias is applied on the horizontal and vertical axis.

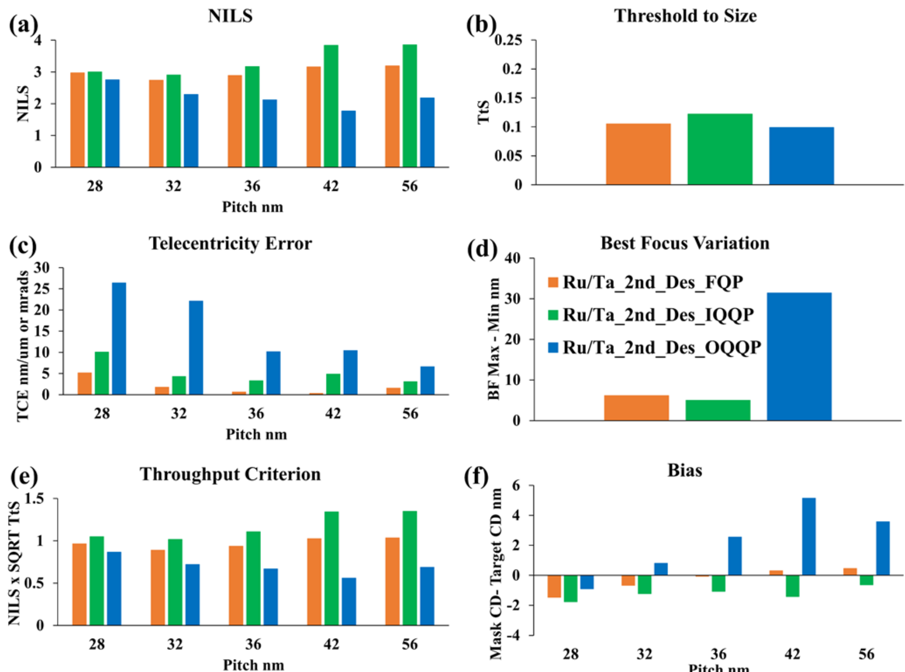

Fig. 11. A through-pitch imaging performance comparison of 2nd Des bilayer stack absorber for contact hole pattern in a square array using different illumination source shapes at NA0.55 (a) NILS, (b) Threshold-to-Size, (c) Telecentricity Error, (d) Best Focus Variation, (e) Throughput Criterion (f) Bias. Imaging metrics are evaluated along the horizontal cutline.

Starting with the NILS plot (Fig. 11(a)), we observe that IQQP demonstrates the highest NILS through pitch followed by FQP, whereas OQQP has the lowest values. As pitch advances, NILS increases for FQP and IQQP, capturing higher diffraction orders. In the case of IQQP, in combination with larger pitches, hardly any part of higher diffraction orders (mainly first

diffraction orders corresponding to pitches under consideration) hits the central obscuration, resulting in higher NILS. Whereas in the case of OHLDP, in combination with larger pitches, some part of higher diffraction orders falls in the central obscuration, resulting in NILS loss. Since FQP comprises IQQP, OQQP, and the other two-quarter parts of the source, the result is expected to lie in between. Unlike LnS patterns, we observe significant improvement in NILS at larger pitches for CH patterns, especially with IQQP, and moderate improvement with FQP.

Comparing NILS values with that of the reference Ta-based absorber (See Supplement 7), the selected Ru/Ta bilayer stack demonstrates around 6% gain at the smallest pitch with IQQP. The gain increases as the pitch grows, reaching up to 18% improvement at pitch 56 nm (IQQP).

Moving on to TtS (Fig. 11(b)), we see that IQQP exhibits the highest TtS followed by FQP, and OQQP has the least among the three illumination sources. Compared to the reference Ta-based absorber (See Supplement 7), TtS values are slightly less. This can be correlated to the mask trench width at which the wafer level target is achieved in the case of the Ru/Ta bilayer stack being slightly less than the reference (Fig. 11(f) and Supplement 7 Fig. S7 (f)).

Turning now to TCE (Fig. 11(c)), FQP demonstrates the least error through pitch, followed by IQQP with maximum error limited to 10 mrad. OQQP shows maximum error, exceeding the recommended value for the smallest pitches.

Next, we shift our attention to BFV (Fig. 11(d)); IQQP exhibits the least BFV followed by FQP. OQQP with around 31 nm of BFV will almost consume the entire focus budget, which is undesired. Compared to the reference Ta-based absorber, Ru/Ta bilayer stacks with FQP and IQQP show a BFV increment of only 2 nm.

Lastly, we arrive at the discussion on TpT (Fig. 11(e)), IQQP with higher NILS values and slightly higher TtS than FQP has the best TpT performance, which is even higher than the reference Ta-based absorber.

Summarizing for CH, IQQP appears to be an optimal choice with maximum NILS through pitch, lowest BFV, and maximum TCE limited to 10 mrad.

4. Conclusion

In this research study, our aim was to identify the optimal combination of Ru/Ta bilayer mask stacks and illumination source shapes to mitigate M3D effects at High-NA 0.55 EUV lithography. Our study provides insight into trade-offs generated due to illumination source shapes so that the industry can make sound choices. Many factors, such as the optical properties of the mask absorber and its thickness, the illumination shape, the pattern's geometry, pitch, and orientation, play a crucial role in determining the EUV imaging performance and exhibit trade-offs. The intricate relationship between the illumination source and the absorber attributes, demands enormous efforts to comprehend EUV imaging. The nonlinearity of the image metrics vs. absorber's optical properties makes it challenging to generalize and predict the behavior and trends in imaging metrics without performing rigorous simulations, making mask absorber studies to be case-specific. Therefore, it is recommended to perform a detailed evaluation of the imaging performance of any proposed novel absorber material to validate its suitability from an imaging standpoint. The findings of this research indicate that the conventional approach of absorber thickness optimization, which solely relies on the literature-recommended values for the absorber reflectivity and phase shift, may not lead to an entirely fair absorber optimization process. The conventional approach fails to acknowledge the impact of many factors that influence imaging metrics, such as the pattern structure, orientation and dimension, mask bias, wafer focus, and illumination source shape. The conventional approach to absorber thickness optimization appears to have become overly reliant on using inductive logic to simplify the task. The underlying assumption is that if a particular factor holds true for absorber A, it must also hold true for absorber B. The suggested notion of an absorber having a certain reflectivity or induced phase shift is based on empirical data, and it may vary depending on the absorber material, the targeted

Optics EXPRESS

dimensions, and the NA of the system. Thus, it is necessary to question whether this approach is truly effective for achieving long-term success. It is important to keep in mind that absorber reflectivity and phase shift values available in the literature are merely suggestions and not absolute. Inputs to simulations, potentially fuelled by experimental characterization, such as precise determination of optical constants, interdiffusion of materials in an absorber stack, oxide formations, and sidewall angle profile, can be helpful to improve the accuracy of the simulation.

A Ru/Ta bilayer absorber stack corresponding to the 2nd order of destructive interference having a 15.3 nm Ru layer on top of a 38.0 nm Ta layer demonstrates optimized imaging performance during the optimal absorber thickness investigation. Imaging metrics unveil a trade-off owing to diffraction order properties. Using an absorber thickness at which the phase difference between the diffraction orders is minimal (cosine of phase difference closer to 1, for the smallest pitch) has shown a reduction in BFV through pitch. We also noticed how the shape of the illumination source influences the imaging metrics, exhibiting trade-offs. A source shape comprising inner sigma source points displayed low TCE. The selected 2nd Des Ru/Ta bilayer stack, in combination with the inner sigma source, results in lower BFV than the reference Ta-based absorber. We understand that the response of two optically different absorber stacks (Ta-based reference absorber and 2nd Des Ru/Ta bilayer absorber) as a function of the line source's sigma position in the illumination is the factor responsible for the observed BFV trends.

At the selected total absorber thickness of 53.3 nm of the Ru/Ta bilayer stack, a full leaf-shaped dipole illumination source shape was found to deliver the most optimal imaging performance for horizontal and vertical line and space patterns, whereas, for contact hole patterns, the inner quarter quasar pole illumination demonstrated optimal through pitch performance. Vertical LnS exhibit improved imaging at thicker Ru/Ta bilayer stack demonstrating imaging trade-offs for horizontal LnS. The recommended notion of opting either inner half or outer half leaf shape for NILS enhancement is only valid at the smallest pitch without any consistent trends in NILS improvement through pitch.

In general, we may conclude that the proposed Ru/Ta bilayer approach demonstrates partial mitigation of M3D effects compared to the reference Ta-based absorber, provided that the appropriate combination of the Ru/Ta bilayer thicknesses and illumination source is identified. It also enhances the flexibility of fine-tuning the optical characteristics through thickness adjustment. The bilayer approach avoids the constraints imposed by the stability of an alloy composition, which is often a limiting factor in single-layer absorbers. Also, the patterning challenge is easily resolved in this particular Ru/Ta bilayer absorber case versus the alloy [15].

When considering the smallest pitches, the imaging performance at high NA 0.55 with Ru/Ta bilayer absorber mask improves compared to the reference Ta-based absorber mask. However, the illumination with complex anamorphic projection employing central obscuration raises concerns for vertical orientation and few specific pitches. Future work could focus on investigating the imaging performance of the proposed absorber masks in a real-case scenario involving tip-to-tip, dense, and isolated patterns in combination with resolution enhancement techniques such as Source Mask Optimization (SMO) and Optical Proximity Correction (OPC). In addition, extending the scope of this study using bright mask tone would be intriguing. Finally, an experimental validation by creating a mask prototype and comparing the performance against the reference Ta-based absorber mask is highly recommended.

Acknowledgments. The authors are grateful to Joern-Holger Franke (imec), Vincent Wiaux (imec), Peter De Bisschop (imec), Lieve Van Look (imec) for the technical discussions and Ulrich Klostermann (Synopsys) for the S-Litho software support.

Disclosures. The authors declare no conflicts of interest.

Data availability. The data that support the findings of this study is available within the paper

Supplemental document. See Supplement 1 for supporting content.

References

1. E. Verhoeven, R. Schuurhuis, M. Mastenbroek, *et al.*, “0.33 NA EUV systems for high volume manufacturing,” in *Extreme Ultraviolet Lithography 2020*, K. G. Ronse, P. A. Gargini, P. P. Naulleau, and T. Itani, eds.(SPIE, 2020).
2. J. Van Schoot, S. Lok, E. van Setten, *et al.*, “High-NA EUV lithography exposure tool: advantages and program progress,” in *Extreme Ultraviolet Lithography 2020*, K. G. Ronse, P. A. Gargini, P. P. Naulleau, and T. Itani, eds. (SPIE, 2021).
3. A. Erdmann, P. Evanschitzky, G. Bottiglieri, *et al.*, “3D mask effects in high NA EUV imaging,” in *Extreme Ultraviolet (EUV) Lithography X*, K. A. Goldberg, ed. (SPIE, 2019).
4. A. Erdmann, H. Mesilhy, P. Evanschitzky, *et al.*, “Perspectives and tradeoffs of absorber materials for high NA EUV lithography,” J. Micro. Nanolithogr. MEMS MOEMS **19**(04), 1 (2020).
5. A. Erdmann, P. Evanschitzky, V. Philipsen, *et al.*, “Attenuated PSM for EUV: Can they mitigate 3D mask effects?” in *Extreme Ultraviolet (EUV) Lithography IX*, N. M. Felix and K. A. Goldberg, eds. (SPIE, 2018).
6. V. Luong, V. Philipsen, E. Hendrickx, *et al.*, “Ni-Al alloys as alternative EUV mask absorber,” Appl. Sci. **8**(4), 521 (2018).
7. D. Thakare, M. Wu, K. Opsomer, *et al.*, “Evaluation of Ta-Co alloys as novel high-k extreme ultraviolet mask absorber,” J. Micro/Nanopattern. Mats. Metro. **22**(02), 1 (2023).
8. M. Burkhardt, “Investigation of alternate mask absorbers in EUV lithography,” in *SPIE Proceedings*, E. M. Panning and K. A. Goldberg, eds. (SPIE, 2017).
9. V. Philipsen, K. V. Luong, L. Souriau, *et al.*, “Reducing extreme ultraviolet mask three-dimensional effects by alternative metal absorbers,” J. Micro. Nanolithogr. MEMS MOEMS **16**(4), 041002 (2017).
10. V. Philipsen, V. Luong, K. Opsomer, *et al.*, “Novel EUV mask absorber evaluation in support of next-generation EUV imaging,” in *Photomask Technology 2018*, J. H. Rankin and E. E. Gallagher, eds. (SPIE, 2018).
11. V. Philipsen, V. Luong, K. Opsomer, *et al.*, “Mask absorber development to enable next-generation EUVL,” in *Photomask Japan 2019: XXVI Symposium on Photomask and Next-Generation Lithography Mask Technology*, A. Ando, ed. (SPIE, 2019).
12. A. Erdmann, D. Xu, P. Evanschitzky, *et al.*, “Characterization and mitigation of 3D mask effects in extreme ultraviolet lithography,” Adv. Opt. Technol. **6**(3-4), 187–201 (2017).
13. M. Wu, D. Thakare, J.-F. de Marneffe, *et al.*, “Study of novel EUVL mask absorber candidates,” J. Micro/Nanopattern. Mats. Metro. **20**(02), 1 (2021).
14. M. Wu, J.-F. de Marneffe, K. Opsomer, *et al.*, “Characterization of $Ru_{4-x}Ta_x$ (x = 1,2,3) alloy as material candidate for EUV low-n mask,” Micro and Nano Engineering **12**, 100089 (2021).
15. D. Thakare, J.-F. de Marneffe, A. Delabie, *et al.*, “Ru/Ta bilayer approach to EUV mask absorbers: Experimental patterning and simulated imaging perspective,” Micro and Nano Engineering **20**, 100223 (2023).
16. D. Thakare, A. Delabie, and V. Philipsen, “Optimizing extreme ultraviolet lithography imaging metrics as a function of absorber thickness and illumination source: a simulation case study of Ta-Co alloy,” J. Micro/Nanopattern. Mats. Metro. **22**(03), 1 (2023).
17. D. Civay, E. Hosler, V. Chauhan, *et al.*, “EUV telecentricity and shadowing errors impact on process margins,” in *SPIE Proceedings*, O. R. Wood and E. M. Panning, eds. (SPIE, 2015).
18. L. de Winter, T. Tudorovskiy, J. van Schoot, *et al.*, “High NA EUV scanner: obscuration and wavefront description,” in *Extreme Ultraviolet Lithography 2020*, K. G. Ronse, P. A. Gargini, P. P. Naulleau, and T. Itani, eds. (SPIE, 2020).
19. I. A. Makhotkin, M. Wu, V. Soltwisch, *et al.*, “Refined extreme ultraviolet mask stack model,” J. Opt. Soc. Am. A **38**(4), 498 (2021).
20. Y. Chen, L. Sun, Z. J. Qi, *et al.*, “Tip-to-tip variation mitigation in extreme ultraviolet lithography for 7 nm and beyond metallization layers and design rule analysis,” J. Vac. Sci. Technol. B Nanotechnol. Microelectron. **35**(6), 1 (2017).
21. G. McIntyre, C.-S. Koay, M. Burkhardt, *et al.*, “Modeling and experiments of non-telecentric thick mask effects for EUV lithography,” in *Alternative Lithographic Technologies*, F. M. Schellenberg and B. M. La Fontaine, eds. (SPIE, 2009).
22. N. V. Davydova, J. Finders, J. McNamara, *et al.*, “Fundamental understanding and experimental verification of bright versus dark field imaging,” in *Extreme Ultraviolet Lithography 2020*, K. G. Ronse, P. A. Gargini, P. P. Naulleau, and T. Itani, eds. (SPIE, 2020).
23. E. van Setten, G. Bottiglieri, L. de Winter, *et al.*, “Edge placement error control and Mask3D effects in High-NA anamorphic EUV lithography,” in *International Conference on Extreme Ultraviolet Lithography 2017*, P. A. Gargini, K. G. Ronse, P. P. Naulleau, and T. Itani, eds. (SPIE, 2017).
24. C. Zahlten, P. Gräupner, J. van Schoot, *et al.*, “High-NA EUV lithography: pushing the limits,” in *35th European Mask and Lithography Conference (EMLC 2019)*, U. F. Behringer and J. Finders, eds. (SPIE, 2019).
25. J.-H. Franke, N. V. Davydova, J. Bekaert, *et al.*, “Tomorrow’s pitches on today’s 0.33 NA scanner: pupil and imaging conditions to print P24 L/S and P28 contact holes,” in *Extreme Ultraviolet Lithography 2020*, K. G. Ronse, P. A. Gargini, P. P. Naulleau, and T. Itani, eds. (SPIE, 2021).
26. J.-H. Franke, J. Bekaert, V. M. Blanco Carballo, *et al.*, “Improving exposure latitudes and aligning best focus through pitch by curing M3D phase effects with controlled aberrations,” in *International Conference on Extreme Ultraviolet Lithography 2019*, K. G. Ronse, P. A. Gargini, P. P. Naulleau, and T. Itani, eds. (SPIE, 2019).
27. M. Burkhardt, Z. G. Chen, S. Halle, *et al.*, “Focus considerations of design pitches and absorber choice for EUV random logic,” in *Optical and EUV Nanolithography XXXV*, A. Lio and M. Burkhardt, eds. (SPIE, 2022).

Optics EXPRESS

28. J. Finders, L. de Winter, and T. Last, "Mitigation of mask three-dimensional induced phase effects by absorber optimization in ArFiand extreme ultraviolet lithography," J. Micro. Nanolithogr. MEMS MOEMS **15**(2), 021408 (2016).
29. A. Grassmann, R. D. Mih, A. Kluwe, *et al.*, "How focus budgets are spent: limitations of advanced i-line lithography," in *Optical Microlithography IX*, G. E. Fuller, ed. (SPIE, 1996).
30. L. S. Melvin, Y. Kandel, T. Fuehner, *et al.*, "Impact of EUV mask absorber sidewall angle on patterning robustness," in *Extreme Ultraviolet (EUV) Lithography IX*, N. M. Felix and K. A. Goldberg, eds. (SPIE, 2018).
31. H. Mesilhy, P. Evanschitzky, G. Bottiglieri, *et al.*, "EUV mask absorber induced best focus shifts," in *Optical and EUV Nanolithography XXXV*, A. Lio and M. Burkhardt, eds. (SPIE, 2022).
32. A. Erdmann, H. Mesilhy, and P. Evanschitzky, "Attenuated phase shift masks: a wild card resolution enhancement for extreme ultraviolet lithography?" J. Micro/Nanopattern. Mats. Metro. **21**, 1 (2022).
33. J. van Schoot, E. van Setten, G. Rispens, *et al.*, "High-numerical aperture extreme ultraviolet scanner for 8-nm lithography and beyond," J. Micro. Nanolithogr. MEMS MOEMS **16**(04), 1 (2017).
34. H. Mesilhy, P. Evanschitzky, G. Bottiglieri, *et al.*, "Investigation of waveguide modes in EUV mask absorbers," J. Micro/Nanopattern. Mats. Metro. **20**(02), 1 (2021).
35. C. van Lare, F. J. Timmermans, J. Finders, *et al.*, "Alternative reticles for low-k1 EUV imaging," in *International Conference on Extreme Ultraviolet Lithography 2019*, K. G. Ronse, P. A. Gargini, P. P. Naulleau, and T. Itani, eds. (SPIE, 2019).